Improved laser-ultrasonic excitation for imaging of seismic physical modeling

Kezhen Jin[1] · Xin Liu[1] · Peilong Li[1] · Qiangzhou Rong[1] · Xueguang Qiao[1]

Abstract

In this study, a laser ultrasonic technology (LUT) was employed for seismic physical model (SPM) imaging. To promote an efficient light-to-ultrasonic-wave conversion, a functionalised Au film was used as a medium because of its stronger photoacoustic (PA) effect. Numerical analysis and experiments were performed to characterise the entire SPM imaging process, including the generation of PA signals, transmission of PA inside the SPM, and collection of echo data for the reconstruction of SPM images using the time-of-flight algorithm. The results show that the Au film coating on the SPM produces a strong PA effect, which significantly improves the imaging depth and resolution of the SPM based on the strong high-frequency ultrasonic wave excitation. The proposed method opens new avenues for SPM imaging using optical technology.

1 Introduction

Seismic physical modelling enables the simulation of the physical aspects of a large-scale natural scenario in a small-scale environment. It is a necessary tool for all the stages in a seismic survey; these stages include the proper configuration of the seismic exploration experiment, signal processing, and seismic data interpretation [1, 2]. The method effectively links computational modelling and field exploration, allowing the conduct of a study in the absence of rock matrix in a nearly ideal setting. Current-driven piezoelectric transducers (PZTs) have been used as the standard source for transmitting ultrasonic waves (UWs) with a frequency of 100 kHz–10 MHz into the seismic physical model (SPM) and detecting their echo from the SPM [3, 4]. The collected seismic data are then reconstructed using the time–light algorithm for SPM imaging. However, the foregoing approach has several inherent disadvantages that should be considered. For instance, large-size structures cause low-efficiency UWs emission into the SPM. The UWs are simply excited but not flexibly controlled; moreover, the narrow

emission band restricts the appropriate restoration of the wide-band information afforded by real seismic explorations.

In this regard, laser ultrasonic technology (LUT) may afford a solution. It is based on the photoacoustic (PA) effect wherein acoustic waves are generated after a material sample absorbs light; this occurs because the optical radiation absorbed by the material is converted to heat [5, 6]. High-power short-pulsed lasers are capable of interacting with the SPM surface and generating thermoelastically induced acoustic waves [7, 8]. The bulk, shear, and surface waves can be simultaneously generated by PA and detected using a microphone or a PZT. The generated UWs may be detected at specific positions, such as at the same side where it was generated, at the back-side of the SPM, or at a certain angle in-between these two aforementioned positions. The spatial resolution and sensitivity to specific feature sizes can also be optimised for a broad range of micro-scale and macro-scale applications. In view of the aforementioned properties, the use of laser-excited UWs is, therefore, an alternative instead of employing a PZT source [9, 10]. However, the pulsed laser usually reaches a high peak power that can easily cause material ablation and damage to the SPM surface. However, if the power of the laser is reduced to realise non-destructive detection, the generated UWs will be extremely weak for transmission into the SPM. Presently, the LUT can only recover micro-structure information on the SPM surface. The key problem is that the light-to-acoustic-wave transformation efficiency is extremely low to derive strong UWs emissions, resulting in poor imaging depth of SPMs,

✉ Xueguang Qiao
xgqiao@nwu.edu.cn

[1] College of Physics, Northwest University, Xi'an, Shaanxi, China

which are normally constructed using organic materials, such as plexiglass and rubber [11, 12].

A solution considered for this problem is the use of functionalised materials as media for improving the PA emission efficiency. To date, diverse advanced materials, such as graphene and its oxides [13], nano-WS$_2$ [14], and carbon nanotubes [15], are used as PA agents and employed in biological imaging. These have exhibited outstanding PA performance and may be used for SPM imaging after solving flexible film generation and achieving low-cost large-scale film generation. The use of PA emissions from noble metal nanoparticles is another attractive approach for generating wideband UWs from wave-emitting devices, i.e., ranging from several hundreds of kHz to several tens of MHz. These emissions may also be utilised for imaging [16] and ultrasonic trapping, which require standing waves in the high-frequency range (> 1 MHz) [17]. Plasmonic gold (Au), especially that with nanoparticle morphology, is widely used as a contrast agent in the thermal expansion-based light-to-acoustic-wave conversion as it affords strong optical absorption when excited at the surface plasmon resonance wavelength [18–20]. Pulsed laser illumination accelerates the reaction of Au particles and increases localised heating, which causes the spontaneous thermal expansion of the surrounding gas. This expanding gas layer acts as an acoustic piston and produces acoustic pressure. The use of two-dimensional (2D) Au films generate PA emission from a well-defined surface, thus allowing the emissions to be distributed over a wide range.

In this study, the LUT technology was used for SPM imaging coupled with the pulsed laser irradiation of samples. To achieve acceptable PA emission performance, the SPM surface was pre-coated with a thin Au film. The acoustic pressure was found to be linearly related to the laser irradiation intensity. The excited UWs were transmitted into the SPM, and the echo signal intercepted by an optical fibre device was reflected back by the inner structures. The seismic data were finally reconstructed using the time-of-flight algorithm for SPM imaging.

2 Theoretical analysis

Assuming that the harmonic frequency (ω) of the time-harmonic electric field (E-field) is under the condition $\left(1/\tau_w\right) \gg \omega$, the E-field ($\vec{E}$) is calculated by the Helmholtz equation [21]:

$$\nabla \times \left(\mu_r^{-1} \nabla \times \vec{E} \right) - k_0^2 \left(\varepsilon_r - j\frac{\sigma}{\omega\varepsilon_0} \right) \vec{E} = 0 \tag{1}$$

where ε_r and ε_0 are the relative and vacuum permittivities, respectively; μ_r, σ, and k_0 are the relative permeability, conductivity, and wave number, respectively.

In the theoretical analysis and simulation, the laser power density at the incidence surface of the absorption layer ($I(t)$)

is simplified to have a Gaussian shape in the time domain. For pulsed laser illumination, the temperature (T) periodically increases and decreases in the Au film and surrounding air, which can be calculated by the following heat diffusion equation:

$$\rho c \frac{\partial T}{\partial t} = \nabla \kappa \nabla T + Q_r^* f\left(\tau_w\right) \tag{2}$$

where $Q_r = \vec{J} \cdot \vec{E}$ is the energy absorbed by Au assuming a non-dissipative host medium; $\vec{J}$ and $\vec{E}$ are the current density and E-field intensity, respectively; ρ, c, and κ are the density, heat capacity, and thermal conductivity, respectively; $f\left(\tau_w\right)$ is the temporal function of the incident laser pulse, as given by the Gaussian profile in [22].

By assuming that only the linear thermal expansion occurs as the temperatures in the Au film and air media increase, the corresponding stress and strain can be evaluated by the Duhamel–Hooke law [23]. The stress tensor, **s**, is related to the second derivative of the structure displacement, **u**, with respect to time and defined at the domain as follows.

$$\nabla \mathbf{s} = \rho \frac{\partial^2 \mathbf{u}}{\partial t^2} \tag{3}$$

Once the model in the boundary between Au and air (i.e., thermal expansion domain) is built, the wave equation describing the pressure distribution versus time and space can be expressed as follows.

$$\frac{1}{\rho v^2} \frac{\partial^2 p_t}{\partial t^2} - \nabla \left(\frac{1}{\rho} \left(\nabla p_t \right) \right) = 0 \tag{4}$$

By solving the above equations, the generated acoustic pressure should follow the function $p_t = A_0 \exp(j\omega t)$, where A_0 is the acoustic pressure amplitude and ω is the angular frequency of acoustic wave oscillation. The mechanism described above is easy to understand and includes three processes: heat conduction, thermal expansion, and acoustic wave generation.

3 Experiment and results

To verify the assumptions, an imaging system with PA generation and UWs detection was developed as shown in Fig. 1. The schematic of the experimental setup, including a 532-nm Nd: YAG nanosecond laser (Coherent) with a pulse duration of 200 ns, repetition rate of 1 kHz, maximum average power of 20 W, and beam diameter of less than 8.5 mm was used as the optical radiation source. The power and size of the laser spot were controlled by the optical attenuator and focusing lens. In the receiving part, the echo was detected by the PZT with a centre resonant frequency of 1 MHz, a
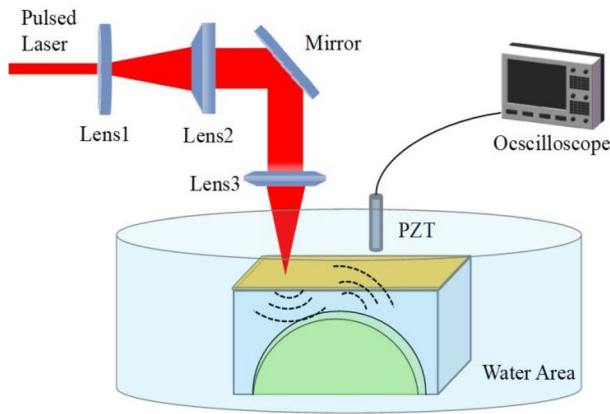
Fig. 1 Schematic diagram of the experimental setup, including two parts of PA generation and UWs detection

diameter of 2 cm, and an aperture of 60°, as shown on the right part of Fig. 1. Here, water acts as the agent to reduce the UWs transmission loss from the model to the PZT.

A 2D cross-sectional representation of the three-dimensional (3D) geometry and boundary conditions of the computational model is used in the simulation. The small arrows in Fig. 2a show the thermal expansion caused by the surrounding medium and Au; the PA pressure is calculated on the outer boundary [24–26]. The simulation of the PA generation process of Au nanoparticles guided the subsequent simulation to a certain extent. As shown in Fig. 2b, a 3D model of polymethyl methacrylate (PMMA), on which the Au film was attached, was built in the water area. The following coupling variables were used. The Gaussian laser pulse was employed as the heat source for the energy transfer of the electromagnetic wave interaction with the Au film. The temperature increase in the Au particle or film and water medium was used as the input in the linear elastic thermal expansion calculations of Au and the water domain in the structural mechanics analysis. The transient temperature distribution was utilised as the input for the structural

mechanics analysis to calculate the strain–stress distribution inside the absorption domain. The acoustic pressure agitated in the outer domain was solved based the pressure acoustic analysis. In the models, setting the boundary conditions was critical to obtain accurate acoustic profiles. Additional boundary and domain conditions were used to truncate the size of the model geometry domain. A perfectly matched layer was set and used to avoid reflection interference in the electromagnetic wave loading. The spherical wave radiation boundary condition was employed in the acoustic pressure generation to allow an outgoing spherical pressure wave to leave the modelling domain with minimal reflections. In the calculations, the typical parameters of the Gaussian pulsed laser (referred to the commercial laser (Nd: YAG Coherent, Evolution) used in the experiment) include the wavelength ($\lambda = 532$ nm), pulse energy ($E = 100$ μJ–20 mJ), laser spot radius ($r = 1$–10 mm), and pulse duration ($\tau_{w} = 200$ ns). Moreover, the Au film parameters used in the models include density (19,300 kg/m^3), Poisson's coefficient (0.42), Young's modulus (78 GPa), linear expansion coefficient (14.2×10^{-6}/K), and heat capacity 129 (J/kg/K). The relevant Au parameters were obtained from an authoritative website, MatWeb, and set in the finite element simulation analysis [27–29].

Once the model was built, the corresponding simulation results were derived, clearly indicating the PA effect of Au acting as the function material for the SPM imaging. The graph of the absorption area spectrum versus different incident laser wavelengths (100–750 nm) is shown in Fig. 3a. The inset indicates the Gaussian-shaped energy density profile of the pulsed laser with a 100 ns pulse width. It establishes a rule that the light absorption capacity of Au is maximum when the surrounding wavelength is approximately 500 nm. To maintain the consistency in the experimental procedure, such as that shown in Fig. 3b, the laser absorption capacity of the Au film was measured; this further demonstrated that different Au films absorbed different laser wavelengths. The pulsed laser wavelength is set at 532 nm in the following simulations and experiments.

Fig. 2 **a** Cross-section analysis of Au nanoparticles, **b** 2D cross-section representation of the 3D geometry and boundary conditions of the computational model. 130 nm Au film is set on polymethyl methacrylate(PMMA)
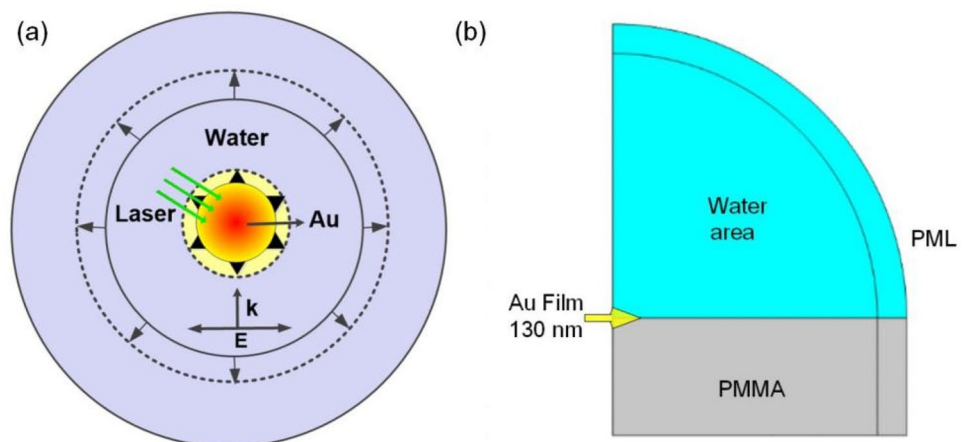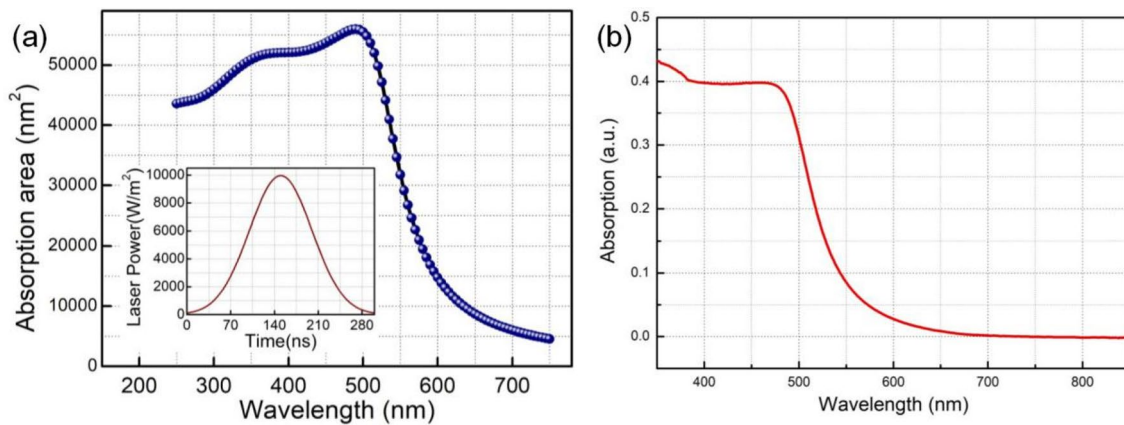
Fig. 3 Au film absorption spectrum, **a** theoretical calculation in absorption Au, where absorption area as a function of the radiated laser wavelength for 130 nm thick Au nanosphere, the inset is the Gaussian pulse laser profile, **b** Experiment test in the optical absorption spectrum of 130 nm Au film

A model of the Au film coated on the PMMA was established using COMSOL Multiphysics. A 532 nm pulsed laser was focused on the Au film surface, causing the local thermal expansion of the gold film surface to act on the PMMA to generate ultrasound. A finite element model was employed to practically evaluate how the material properties and dimensions affected the PA generation when the boundary constraint was afforded by water (Fig. 4a). In Fig. 4b, c, the influence of power on the PA signal intensities of the Au and Ag films were separately simulated using the same power. The figure indicates that the PA signals increase as the excitation power increases from 1 to 3 W, clearly demonstrating that laser power has an important function in the PA signal generation. With the same laser power, if the Au film is replaced by the Ag film, the latter also exhibits the PA effect but is 10 times more intense than that of the former, as shown in Fig. 4c, d.

The SPM imaging is simulated in this study using pulsed UWs as a source and a detector to intercept the echo data from multiple interfaces inside the model [30–33]. It is commonly acknowledged that the acoustic wave evolves into several waves (e.g., body and surface waves) as it travels in the solid bulk, especially through the crack regions inside the model. This is because, in the experiment, the echo data were intercepted with water as the coupling agent; hence, only the longitudinal wave was detected by the PZT. Accordingly, only the longitudinal wave was considered in acoustic wave travel and echo detection. Then, an uplifting SPM with an inverted curve profile was built. The SPM material was plexiglass, which has a low acoustic impedance and a scale of several centimetre. The acoustic source was set at the SPM surface, and it radiated a 300 kHz pulsed UW into the model. The sensor was also installed on the SPM surface 5 cm away from the acoustic source. The simulated UWs travel and reflection contours are shown in Fig. 5a, b, , where

the partial UW is reflected in the interface of the uplifting region. The time-domain signal of the echo is shown in Fig. 5c, where the time delay between two signal peaks corresponds to the position of the reflecting surfaces. Then, the source and sensor were controlled to move along the surface at 2-mm intervals, simulating the scanning detection process. The echo signals indicate the different arrival times (Fig. 5d, i.e., the time delays in the arrival of information containing the position of the arched contour. As expected, after the seismic data reconstruction using the inverse time algorithm, the uplifting interface profile inside the SPM was clearly observed (Fig. 5e).

As mentioned above, PA excitation is relative to multiparameters, such as excitation laser fluence, light absorption of target material mentioned above, and surround ambient of target. Considering our application in SPM imaging, 130 nm thick gold film was employed, and the test sample was placed in the water. Experiments were performed to evaluate the PA generation efficiency of Au film under different excitation laser energy. The gold film was attached to a plexiglass surface, and its PA signal was detected using the PZT. In Fig. 6a, several bipolar UWs signals were observed as the laser radiated on the SPM surface with the power ranging from 7.70 to 13.00 W. The shape of the head wave was consistent with the theoretical simulation, and the extra tail oscillation was caused by the aftershocks in the Au film; the laser power increased with the UWs signals intensity. The peak-to-peak voltage of the UWs signals was recorded and plotted as the function of laser power, as shown in Fig. 6b. The figure clearly shows that the excited UWs pressure is linear relative to the low laser power. This experiment well identified the PA performance of the Au film. In the following experiment, the Au film was employed as the medium to improve the ultrasonic laser emission on the SPM surface [34, 35].
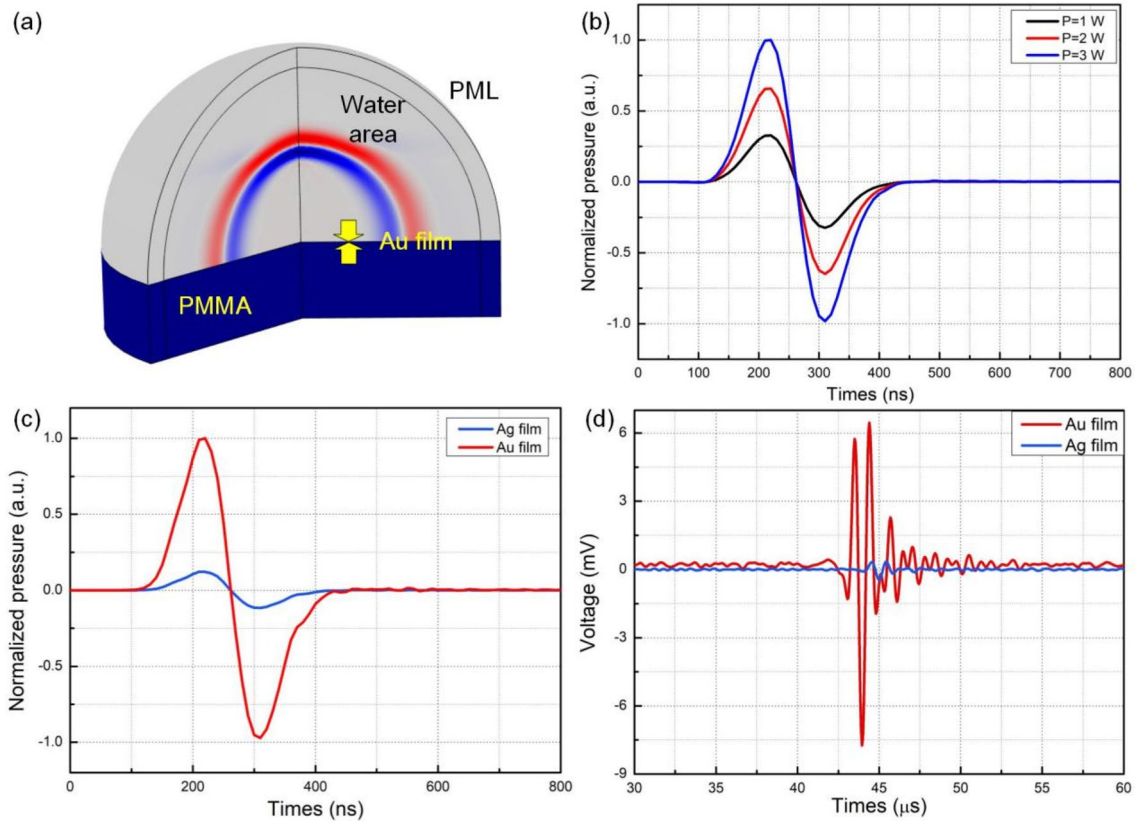
Fig. 4 **a** The ultrasonic excitation generation in 3D model, **b** UWs signal simulation by increasing excitation laser power, **c** Compare PA effects of both Au film and Ag film in simulation, **d** Experimental testing of PA effects of both Au film and Ag film
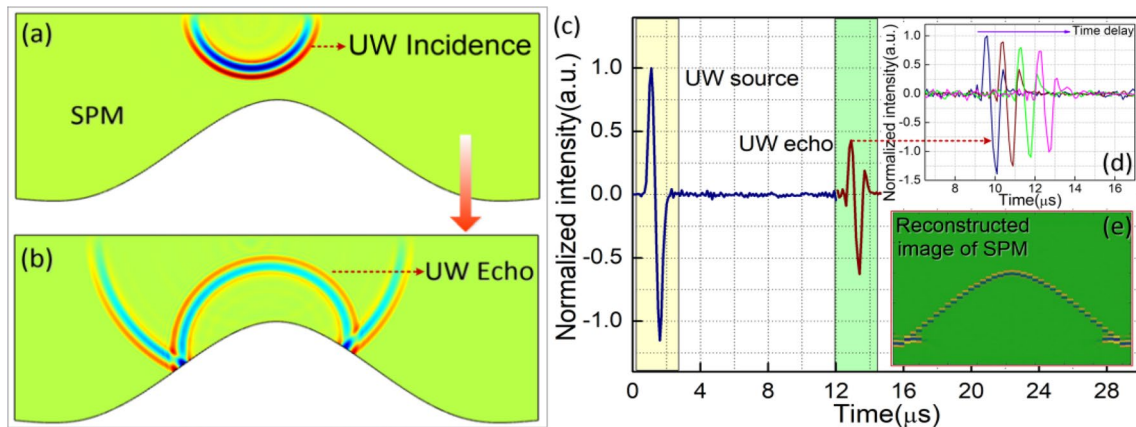

Fig. 5 Numerically simulated SPM imaging, **a** the PA transmits into SPM, **b** the partial UW was reflected by the inside arched profile, **c** the recorded echo signals including the direct wave signal and the structure signal, **d** the time delay of echo from the reflections of different positions on the surface of the inside structure, and **e** the reconstructed image of SPM by the time-of-flight algorithm

The SPM imaging system includes two parts of the laser: UWs emission and UW detection, as shown in Fig. 7. Two SPMs were fabricated using the 3D-printing technology, which simulated two simple geological structures (i.e., sunken and arched structures in natural scenarios); the material used was plexiglass with a low acoustic impedance in water. Unlike the traditional fabrication method, the material was flexibly selected, and micro-scale geological structures were more accurately prepared.
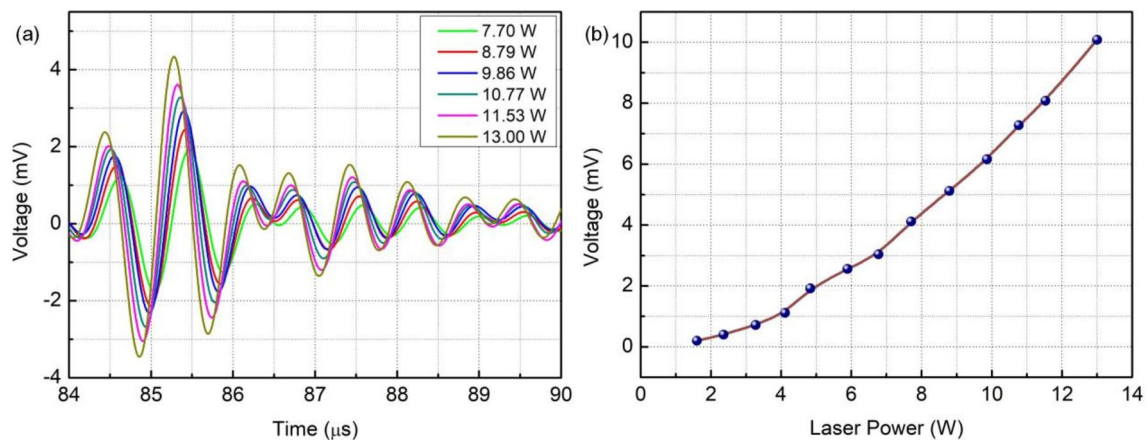
Fig. 6 PA signals of Au film, **a** the time-domain pulse signal with the different laser power, **b** the signal peak as the function of laser power

**Fig. 7** Photographs of two SPMs with Au film coating
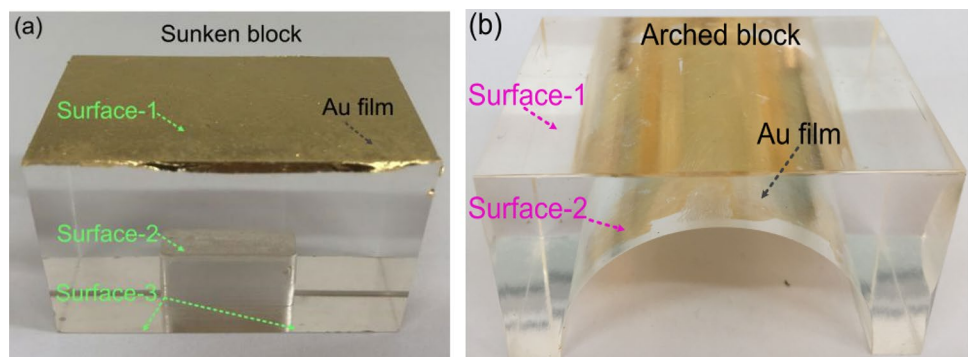
The SPM surfaces were smoothed and cleaned well to ensure that the nano-thick (130 nm) Au films were securely attached: the upper and bottom areas of the sunken and arched SPM surfaces were gold-coated. The attachment process was simple because it only involved placing the Au film on the surfaces and then allowing the Van der Waals' force to cause the film to tightly adhere [36]. The prepared SPMs (Fig. 7) were placed into a water tank for laser irradiation. A focusing PZT was hanged over the model, and its bottom surface was immersed in water.

To further characterise the influence of laser radiation on the UWs generation, the laser was modulated into two shapes: circle (with a diameter of 4 mm) and rectangle (with a width of 4 mm and length of 8 mm). Their UWs signals were recorded as functions of the laser power, as shown in Fig. 8a. It is clearly observed that regardless of the laser shape, the UWs signals first increase monotonously before reaching the maximum because of the light-to-acoustic-wave transferring saturation. It is also found that UWs signal fluctuations appear on the saturation regions of the two curves; this is mainly attributed to the air bubble generation on the Au film when the laser power is sufficiently high. As the laser power significantly increases, both the Au film and model burn and break, resulting in the disappearance of UWs signals. This observation may be used as a valuable reference for choosing the appropriate level of laser power. Moreover, the result shows that the UWs generated by the rectangular laser was stronger than that of the circular laser. It is evident that more intense UWs are generated by the larger laser.

The Au film surface was irradiated to generate the UWs at the same laser power. In the SPM imaging process, the rectangular laser beam with a larger illumination surface was, therefore, used as the radiation source; the laser power was set as 9 W.

When the laser irradiated the Au film, the UWs were generated and transmitted into the SPM material; a high-speed data acquisition card was used to transfer the seismic signals. The echo signal in the time domain when the sunken model was irradiated is shown in Fig. 8b; it contains two waves of the UWs reflected by the upper and bottom surfaces of the model. The time gap between the two reflected signals can be used to obtain the relative position information on the two surfaces according to the UWs propagation velocity in the SPMs.
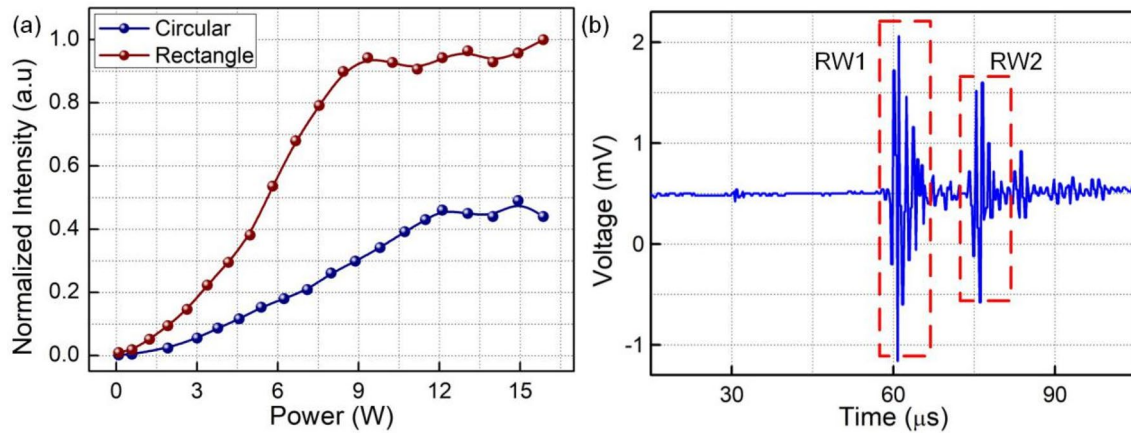
Fig. 8 **a** UWs signals generated by the different laser shape and power, **b** Photoacoustic echo time-domain signal collected from the sunken SPM

For the imaging of the two SPMs, the laser source and PZT were placed in the same moving stage with a fixed distance to move together and scan the models. The echoes were collected and recorded in real-time using an interrogation system. The 2D images of the SPMs were reconstructed by the reverse time algorithm. The profiles of the SPM edges were observed in the 2D images, as shown in Fig. 9. As mentioned, for the sunken block SPM, the upper surface of the Au film was coated, and the UWs were excited; the partial UWs energy was directly reflected by the upper surface to the PZT and transmitted into the SPM. The UWs were reflected by the inner interface inside the SPM. After data reconstruction, the two interfaces were clearly observed in the image. The imaging contrast ratio of the two interfaces was only determined by UWs generation and transmission loss. For the arched block SPM, the bottom surface of the Au film was coated, and the UWs were excited on both the upper and bottom surfaces. Because of the low PA efficiency of the SPM, the UWs on the upper surface was weakly excited. In

contrast, the light passed through the SPM and irradiated the Au film, exciting a strong UW that propagated back to the PZT. As a result, the bottom surface image was considerably clearer than that of the upper surface. This indicated that the Au film was an acceptable medium for improving the SPM imaging effect.

4 Conclusion

In this study, an LUT-based SPM imaging method was implemented in the theoretical analysis and experimental demonstration. An Au film was used to considerably improve the PA generation on the SPM surface. By adjusting the laser power, different UWs pressure can be generated, making the UWs generation more flexible as a result of the acceptable thermal stability of the Au film. By detecting the seismic echo data, the two SPMs were clearly imaged by reconstructing the recorded echo signals. This approach
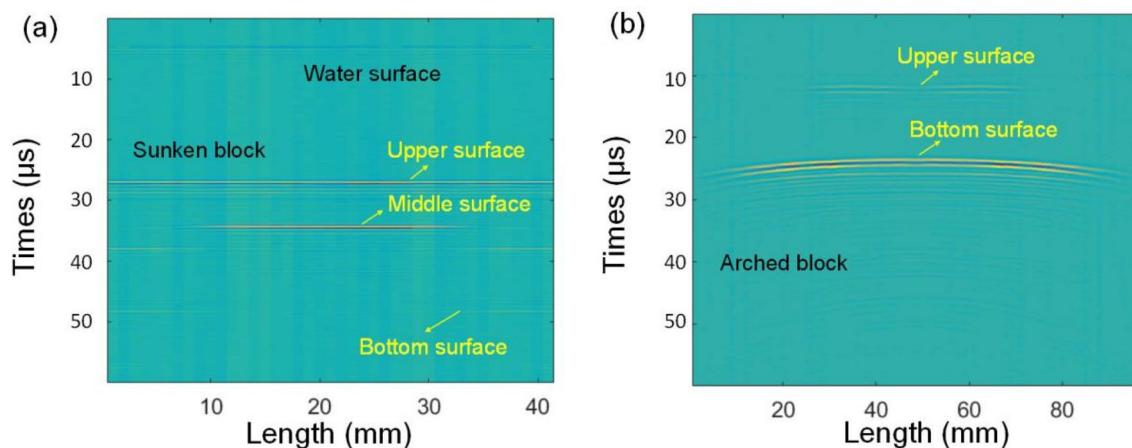
Fig. 9 Reconstructed images of two SPMs, **a** sunken block, **b** arched block

is satisfactory for promoting the LUT to achieve deep and high-resolution SPM imaging.

References

1. M.S. King, Rock-physics developments in seismic exploration: a personal 50-year perspective. Geophysics **70**(6), 3ND-8ND (2005)

2. L.K. Santos, Seismic physical modeling based on the physical similitudes: application in isotropic media. Master's Dissertation, Federal University of Pará, 2015

3. T.R. Gururaja, W.A. Schulze, L.E. Cross, R.E. Newnham, B.A. Auld, Y.J. Wang, Piezoelectric composite materials for ultrasonic transducer applications. Part I: resonant modes of vibration of PZT rod-polymer composites, IEEE Trans. Sonics Ultrason. **32**(4) (1995)

4. J. Jung, V. Annapureddy, G.-T. Hwang, Y. Song, W. Lee, W. Kang, J. Ryu, H. Choi, 31-mode piezoelectric micromachined ultrasonic transducer with PZT thick film by granule spraying in vacuum process. Appl. Phys. Lett. **110**, 212903 (2017)

5. C.B. Scruby, Some applications of laser ultrasound. Ultrasonics **27**(4), 195–209 (1989)

6. T. Liu, J. Wang, G.I. Petrov, V.V. Yakovlev, H.F. Zhang, Photoacoustic generation by multiple picosecond pulse excitation. Med. Phys. **37**(4), 1518–1521 (2010)

7. C.B. Scruby, Some applications of laser ultrasound. Ultrasonics **27**, 195–209 (1989)

8. Y. Li, J. Tian, S. Ji, C. Zhou, Y. Sun, Y. Yao, Fiber-optic multipoint laser-ultrasonic excitation transducer using coreless fibers. Opt. Express **27**(5), 6116–6128 (2019)

9. B. Pouet, P.N.J. Rasolofosaon, Seismic physical modeling using laser ultrasonics, *Society of Exploration Geophysicists*, 1990 SEG Annual Meeting, (1990), pp.841–844

10. I. Arias, Modeling of the detection of surface-breaking cracks by laser ultrasonics, Doctor of Philosophy Dissertation, Northwestern University, 2003

11. R.G. Pratt, Seismic waveform inversion in the frequency domain, Part 1: theory and verification in a physical scale model. Geophysics **64**(3), 888–901 (1999)

12. Q. Rong, Z. Shao, X. Yin, T. Gang, F. Liu, A. Sun, X. Qiao, Ultrasonic imaging of seismic physical models using fiber bragg grating fabry-perot probe. IEEE J. Sel. Top. Quant. Electron. **23**(2), 560056 (2017)

13. Y.W. Wang, Y.Y. Fu, Q.L. Peng, S.S. Guo, G. Liu, J. Li, H.H. Yang, G.N. Chen, Dye-enhanced graphene oxide for photothermal therapy and photoacoustic imaging. J. Mater. Chem. B **1**, 5762–5767 (2013)

14. G.B. Yang, H. Gong, T. Liu, X.Q. Sun, L. Cheng, Z. Liu, Two-dimensional magnetic $WS_2@Fe_3O_4$ nanocomposite with mesoporous silica coating for drug delivery and imaging-guided therapy of cancer. Biomaterials **60**, 62–71 (2015)

15. A. Zerda, Z. Liu, S. Bodapati, R. Teed, S. Vaithilingam, B.T. Khuri-Yakub, X.Y. Chen, H.J. Dai, S.S. Gambhir, Ultra-high sensitivity carbon nanotube agents for photoacoustic molecular imaging in living mice. Nano Lett. **10**(6), 2168–2172 (2010)

16. K. Homan, J. Shah, S. Gomez, H. Gensler, A. Karpiouk, Silver nanosystems for photoacoustic imaging and image-guided therapy, J. Biomed. Opt. **15**(2) (2010)

17. J. Lee, S-Y. Teh, A. Lee, H.H. Kim, C.Y. Lee, K.K. Shung, Transverse acoustic trapping using a Gaussian focused ultrasound, Ultrasound Med. Biol. **36**(2) (2010)

18. A. Hatef, B. Darvish, A. Dagallier, Y.R. Davletshin, W. Johnston, J.C. Kumaradas, D. Rioux, M. Meunier, Analysis of photoacoustic response from gold-silver alloy nanoparticles irradiated by short pulsed laser in water. J. Phys. Chem. C **119**(42), 24075–24080 (2015)

19. W.W. Li, X.Y. Chen, Gold nanoparticles for photoacoustic imaging. Nanomedicine **10**(2), 299–320 (2015)

20. F.C.P. Masim, W.-H. Hsu, H.-L. Liu, T. Yonezawa, A. Balcytis, S. Juodkazis, K. Hatanaka, Photoacoustic signal enhancements from gold nano-colloidal suspensions excited by a pair of time-delayed femtosecond pulses. Opt. Express **25**(16), 19497–19507 (2017)

21. E.P. Furlani, I.H. Karampelas, Q. Xie, Analysis of pulsed laser plasmon-assisted photothermal heating and bubble generation at the nanoscale. Lab Chip **12**, 3707–3719 (2012)

22. A.O. Govorov, W. Zhang, T. Skeini, H. Richardson, J. Lee, N.A. Kotov, Gold nanoparticle ensembles as heaters and actuators: melting and collective plasmon resonances. Nanoscale Res. Lett. **1**, 84–90 (2006)

23. L-H.V.Wang, Photoacoustic iImaging photoacoustic imaging and spectroscopy, *CRC Press*, TAYLOR & Francis Group, Boca Raton, London, New York, 2009

24. F. Gao, R. Kishor, X. Feng, et al., An analytical study of photoacoustic and thermoacoustic generation efficiency towards contrast agent and film design optimization, Photoacoustics (2017)

25. X. Liu, W. Wang, Q. Rong, B. Yu, Highly sensitive photoacoustic imaging: a new strategy for ultrahigh spatial resolution seismic physical model imaging. IEEE Photonics J. **12**(3), 1–11 (2020)

26. H. Chen, X. Qiao, F. Chen et al., Photoacoustic generation using WS2 in ultrasonic detection of seismic physical models. Opt. Int. J.Light Electr. Opt. **200**, 163401 (2019)

27. C. Noguez, Surface plasmons on metal nanoparticles: the influence of shape and physical environment. J. Phys. Chem. C **111**(10), 3806 (2007)

28. M.A. Garcia, Surface plasmons in metallic nanoparticles: fundamentals and applications. J. Phys. D Appl. Phys. **44**(28), 283001 (2011)

29. S.Y. Gezgïn, H.Ş. Kılıç, An improvement on the conversion efficiency of Si/CZTS solar cells by LSPR effect of embedded plasmonic Au nanoparticles, **101** (2020)

30. T. Gang, M. Hu, X. Qiao, J. Li, Z. Shao, R. Tong, Q. Rong, Fiber-optic Michelson interferometer fixed in a tilted tube for direction-dependent ultrasonic detection. Opt. Laser Eng. **88**, 60–64 (2017)

31. Z. Shao, Q. Rong, F. Chen, X. Qiao, High-spatial-resolution ultrasonic sensor using a micro suspended-core fiber. Opt. Express **26**(8), 10820–10832 (2018)

32. X. Qiao, Z. Shao, W. Bao, Q. Rong, Fiber Bragg grating sensors for the oil industry. Sensors **17**(3), 429 (2017)

33. Y. Tian, N. Wu, K. Sun et al., Numerical simulation of fiber-optic photoacoustic generator using nanocomposite material. J. Comput. Acoust. **21**(2), 1350002 (2013)

34. I.G. Calasso, W. Craig, G.J. Diebold, Photoacoustic point source. Phys. Rev. Lett. **86**(16), 3550 (2001)

35. G.J. Diebold, The photoacoustic effect generated by a spherical droplet in a fluid. J. Acoust. Soc. Am. **84**(6), 2245–2251 (1988)

36. J.H.D. Boer, J.F.H. Custers, Adsorption by van der Waals forces and surface structure. Physica **4**(10), 1017–1024 (1937)